Journal of
Materials Chemistry A

PAPER

View Article Online
View Journal

Cite this: DOI: 10.1039/d6ta02867e

Photothermal-stable flexible perovskite solar cells enabled by PbI_2 suppression with amino-functionalized graphene quantum dots

Hao Wang, Xiaoran Li, Wei Yu and Xin Li *

Received 5th April 2026
Accepted 29th May 2026

DOI: 10.1039/d6ta02867e

rsc.li/materials-a

The upper interface of inverted flexible perovskite solar cells (FPSCs) is prone to degradation under photothermal stress, leading to the formation of lead iodide (PbI_2) that severely compromises both device efficiency and operational stability. Herein, we propose amino-functionalized graphene quantum dots (A-GQDs) as a versatile upper interface modifier to address this critical challenge. The abundant Lewis base groups on A-GQDs establish strong coordinated bonding with uncoordinated Pb^{2+} and form synergistic hydrogen bonding networks with iodide ions and organic cations, enabling effective defect passivation, favorable energy level alignment, and substantial residual stress release. Remarkably, the A-GQDs layer consistently inhibits photothermal-induced PbI_2 generation and effectively blocks ionic migration during device operation. Benefiting from this multifunctional interface engineering, the optimized flexible devices achieve a champion power conversion efficiency (PCE) of 23.11%, along with exceptional stability under continuous photothermal aging, mechanical bending, and damp heat exposure. This work presents a new interfacial engineering paradigm that synergistically integrates defect passivation, stress relief, and synergistic stabilization for high-performance flexible photovoltaics.

1. Introduction

Flexible perovskite solar cells (FPSCs) have emerged as core candidates for next-generation portable and wearable energy technologies, owing to their exceptional power-to-weight ratio, superior bending durability, and promising roll-to-roll manufacturing compatibility. However, their commercial viability remains constrained by the critical bottleneck of insufficient long-term operational stability.[1–3] Compared to rigid substrates, flexible plastic substrates (*e.g.*, PET, PEN) suffer from intrinsic shortcomings including coefficient of thermal expansion mismatch, low thermal conductivity, and high surface roughness. These inherent drawbacks render the perovskite films deposited thereon more susceptible to synergistic degradation under coupled photo-thermal, moisture, oxygen, and mechanical stresses.[4,5] Notably, the upper interface between the perovskite active layer and the top electron transport layer represents the most vulnerable region where defect accumulation, ion migration, and stress-induced lattice distortion are most pronounced, ultimately dictating both device efficiency and stability.[6,7] Consequently, developing robust upper interface passivation strategies capable of withstanding dynamic stresses is imperative for achieving synergistic enhancement of high performance and reliability in FPSCs.

In inverted (p–i–n) perovskite solar cells, upper interface engineering is primarily directed toward three concurrent objectives: (1) effective chemical and electronic defect passivation, (2) optimization of energy level alignment to facilitate electron extraction, and (3) suppression of interfacial ion migration and phase segregation.[8] In recent years, diverse material systems for upper interface passivation have been extensively explored. For instance, organic small-molecule ammonium salts such as propane-1,3-diamine iodide ($PDAI_2$)[9] and phenethylammonium chloride (PEACl)[10] have been widely employed for shallow-level defect passivation through efficient coordination with undercoordinated Pb^{2+} ions, effectively mitigating non-radiative recombination losses and substantially enhancing open-circuit voltage. Functionalized polymers, including 1,3-bis(2-vinylbenzyl)-1*H*-benzimidazolium chloride (PVBN)[11] and dithienylpyrazinediimide-bithiophene imide (TPDI-BTI),[12] serve as physical capping layers that stabilize the perovskite interface while simultaneously improving contact with fullerene-based electron transport layers. Inorganic materials, such as atomic-layer-deposited AlO_x,[13] PbTe,[14] and titanium carbide MXene ($Ti_3C_2T_x$),[15] benefit from lattice compatibility and favorable energy alignment with perovskites, making them promising candidates for interfacial epitaxial growth layers that enhance charge extraction and improve device environmental tolerance. Collectively, these efforts have established "chemical interfacial modification" and "physical barrier construction" as two fundamental paradigms for elevating upper interface quality.

School of Electronic Science and Engineering, Xiamen University, Xiamen 361005, China. E-mail: lixin01@xmu.edu.cn

Despite significant progress, growing concerns have emerged regarding the fundamental inadequacies of existing upper interface passivation strategies when applied to FPSCs. First, most passivating agents, particularly organic small molecules, exhibit static and passive interactions. While effective in passivating pre-existing defects formed during fabrication, the passivation ability is limited under the condition of continuous external stress, especially under permanent photothermal stress.[16,17] Second, many materials—such as certain inorganic compounds or rigid polymers—may improve electron transport but suffer from inherent brittleness or thermomechanical mismatch with the perovskite lattice, potentially becoming nucleation sites for microcrack formation under bending stress, thereby compromising mechanical reliability. Most critically, the vast majority of strategies neglect to directly intervene in the core degradation pathway of perovskites under photothermal stress, namely the formation and accumulation of lead iodide (PbI_2).[18,19] PbI_2 not only acts as a non-radiative recombination center but also accelerates interfacial delamination and performance decay upon accumulation.[20] Therefore, the development of novel upper interface materials that can dynamically accommodate flexible substrate deformation, actively suppress degradation product formation, and simultaneously fulfill multiple passivation functions represents an urgent imperative for achieving substantive breakthroughs in FPSCs.

Among various emerging interface materials, graphene quantum dots (GQDs) have demonstrated great potential as ideal interfacial modifiers owing to their abundant surface functional groups, excellent solution processability, and good mechanical flexibility. To date, the application of GQDs in perovskite solar cells (PSCs) has been extensively explored; however, most studies focus on conventional n–i–p structured rigid PSCs (RPSCs), where GQDs are primarily positioned at the electron transport layer/perovskite interface (ETL/PVK) or used as additive in the perovskite bulk. For instance, Xie *et al.* modified the SnO_2 ETL with GQDs, which enhanced electron extraction and suppressed interfacial recombination, achieving a power conversion efficiency (PCE) of 20.23%.[21] Subsequently, Pang *et al.* modified SnO_2 by GQDs, further increasing the PCE to 21.1%.[22] Gao *et al.* designed imidazole bromide-functionalized GQDs (I-GQDs) for the SnO_2/PVK interface, reaching a PCE of 22.37%.[23] Zhou *et al.* prepared GQD and SnO_2 nanoparticle composites (G@SnO_2) as ETLs to RPSCs and FPSCs, achieving PCE of 19.6% and 17.7%, respectively.[24] In addition, GQDs have been used as bulk additives in n–i–p PSCs: Hu *et al.* incorporated F/N-codoped GQDs into carbon-based PSCs (CPSCs) and use it as the post-treatment agent, improved thermal stability but yielded a moderate PCE of 16.37%.[25] Chen *et al.* introduced fluorinated GQDs (FGQDs) into the anti-solvent, and the FGQDs-optimized RPSCs delivered the PCE of 24.12%.[26] Yang *et al.* introduced fluorographene quantum dots (FGQDs) into the bulk perovskite phase, achieving the PCE of 20.4% in FPSCs.[27] In contrast, the utilization of GQDs in inverted (p–i–n) PSCs has been rarely reported. Shin *et al.* employed GQDs as hole transport layer (HTL) to replace poly(3,4-ethylenedioxythiophene):polystyrene sulfonate (PEDOT:PSS).[28] In combination with graphene transparent electrodes, they achieved efficiencies of 15.38% for FPSCs and 17.15% for RPSCs, respectively. Khan *et al.* employed N-doped GQDs as an interlayer positioned between PVK/ETL to passivate defects and suppress recombination, the resulting RPSCs efficiency remained 17.10%.[29] Gan *et al.* employed graphite-nitrogen doped GQDs (GN-GQDs) as bulk additive, achieving the PCE of 19.8% fot RPSCs.[30] Notably, none of the aforementioned studies on GQDs-based interface engineering or bulk doping provides a systematic assessment of device stability, particularly regarding the specific role of GQDs in bolstering long-term operational resilience under coupled photothermal stress, which is a critical bottleneck that must be addressed to enable the practical deployment of PSCs. Furthermore, in the context of inverted FPSCs, there remains considerable scope for further enhancements in both PCE and operational stability through the judicious incorporation of GQDs.

In response to these challenges, this work innovatively proposes and systematically validates a versatile upper interface reinforcement strategy for FPSCs, employing amino functionalized graphene quantum dots (A-GQDs) as an “intelligent” modifier layer positioned between the perovskite and electron transport layer. This design ingeniously integrates the size advantages of zero-dimensional quantum dots with the chemical reactivity of surface amino groups. On one hand, the amino groups, functioning as strong Lewis bases, effectively anchor undercoordinated Pb^{2+} and iodide vacancies at the perovskite surface and grain boundaries, achieving excellent static passivation. On the other hand, we discover A-GQDs act as a “healing agent” under continuous photothermal stress, effectively inhibiting the crystallization and aggregation of deleterious lead iodide, thereby fundamentally mitigating interfacial degradation. Through comprehensive electrochemical characterization and microstructural analysis, this work provides compelling evidence that this strategy not only markedly enhances the PCE of flexible devices but also endows them with exceptional stability under maximum power point (MPP) tracking, photothermal aging, and bending cycling tests, substantially outperforming control devices. The detailed comparison of this work with previous GQDs/graphene studies in PSCs is provided in Table S1. This study offers a novel and efficient material pathway toward resolving the long-standing challenge of interfacial dynamic instability in flexible perovskite photovoltaics.

2. Results and discussion

2.1 Characterization of A-GQDs

The morphology, structure, chemical composition, and fabrication process of the A-GQDs were systematically characterized to establish their fundamental physicochemical properties as an efficient interface modification material. Fig. 1a–c present the morphology and size distribution of A-GQDs. Transmission electron microscopy (TEM) imaging (Fig. 1a) clearly reveals that the A-GQDs exhibit excellent monodispersity without noticeable aggregation. High-resolution TEM (HRTEM, Fig. 1b) further

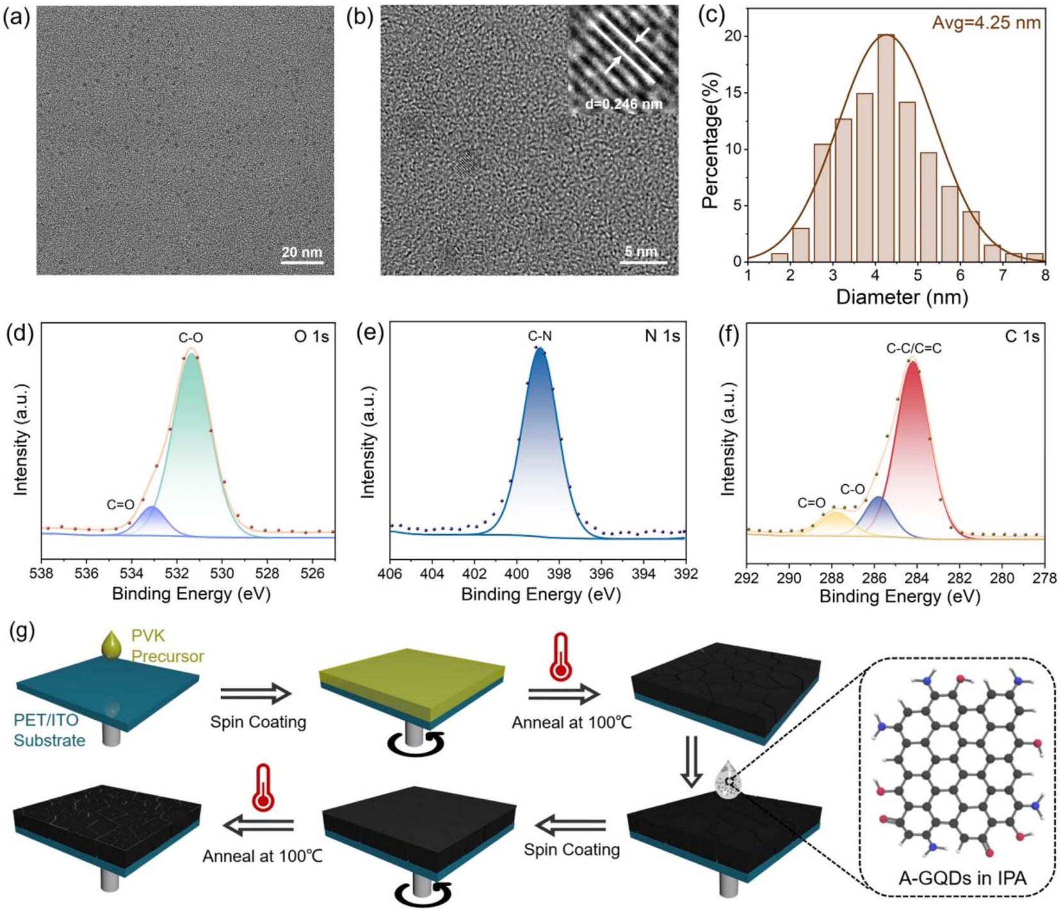

Fig. 1 (a) TEM image of A-GQDs. (b) High-resolution TEM images of A-GQDs. (c) Particle size distribution diagram of A-GQDs. XPS spectra of (d) C 1s, (e) O 1s and (f) N 1s of A-GQDs. (g) Schematic diagram of preparation process for A-GQDs modified perovskite film.

resolves the crystalline structure of an individual quantum dot, displaying well-defined lattice fringes with an interplanar spacing of approximately 0.246 nm. Statistical analysis of the A-GQDs size distribution (Fig. 1c) yields an average diameter of 4.25 ± 0.68 nm. This uniform nanoscale dimension is critical for forming continuous, pinhole-free ultrathin modification layers on rough flexible perovskite film surfaces, facilitating homogeneous interfacial interactions and efficient charge transport.[31]

To gain deeper insight into the surface chemical functionalities of A-GQDs, X-ray photoelectron spectroscopy (XPS) analysis was performed, with results shown in Fig. 1d–f. The C 1s spectrum (Fig. 1d) can be deconvoluted into three characteristic peaks: the dominant peak at 284.2 eV is assigned to sp^2-hybridized C–C/C=C bonds, confirming the presence of the graphene sp^2 carbon framework, and peaks at 285.8 eV and 287.7 eV correspond to C–O and C=O bonds, respectively. The O 1s spectrum (Fig. 1e) exhibits fitted peaks at 531.3 eV (C=O) and 533.0 eV (C–O), corroborating the C 1s analysis. Most importantly, the N 1s spectrum (Fig. 1f) displays a single symmetric peak at 398.9 eV, attributable to C–N bonds, providing direct evidence for the presence of amino (–NH$_2$) functional groups on the graphene quantum dot surface.[32] The abundant oxygen- and nitrogen-containing functional groups not only ensure excellent dispersibility of A-GQDs in polar solvents but also furnish active sites for interacting with perovskite components and achieving defect passivation. Fourier-transform infrared (FT-IR) spectroscopy further corroborates the existence of these surface functional groups (Fig. S3), while schematic structural representations and simplified models of A-GQDs are presented in Fig. S1 and S2, respectively.

As illustrated in Fig. 1g, a stable A-GQDs modification layer was formed by directly depositing an A-GQDs solution in isopropanol (IPA) onto the as-prepared perovskite film surface *via* a one-step spin-coating method, followed by a mild annealing treatment. This fabrication protocol is perfectly compatible with the low-temperature processing requirements of inverted FPSCs, offering significant advantages in terms of cost and manufacturability, and presenting a viable technological pathway toward large-scale production of high-performance flexible devices.

2.2 Interfacial interaction mechanism between A-GQDs and perovskite films

To elucidate the fundamental role of A-GQDs as an interfacial modifier, the physical and chemical interactions between A-GQDs and the perovskite film are systematically investigated.

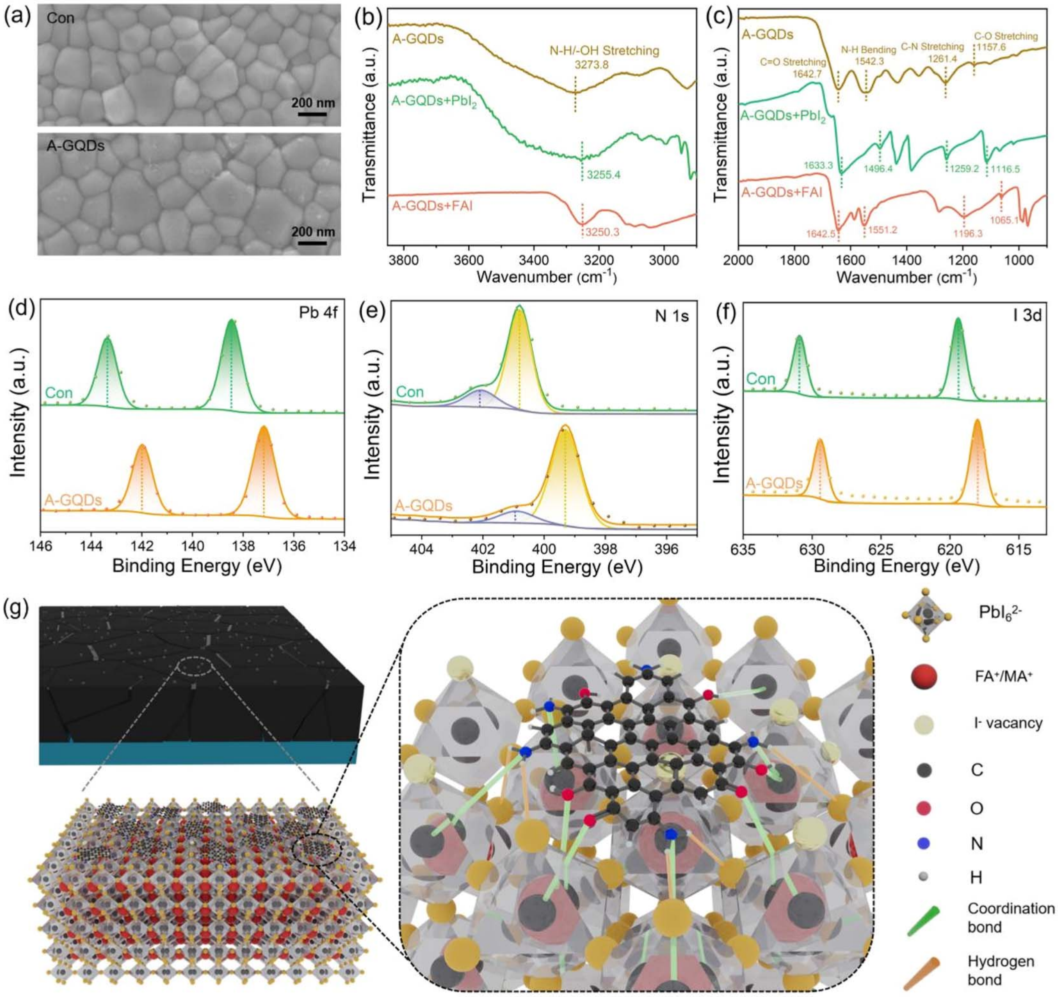

Fig. 2 (a) SEM images of perovskite films without and with A-GQDs modified. (b and c) FT-IR spectra of A-GQDs, A-GQDs and PbI$_2$ mixture, A-GQDs and FAI mixture. XPS spectra of (d) Pb 4f, (e) N 1s and (f) I 3d without and with A-GQDs modified perovskite films. (g) Schematic diagram of interaction mechanism between A-GQDs and perovskite film.

Fig. 2a presents scanning electron microscopy (SEM) images (50 k × magnification) comparing the surface morphology of pristine (Control) and A-GQDs-modified perovskite films. A uniform coverage of nanoparticles is clearly observed on the modified film surface, providing direct evidence for the successful deposition of the A-GQDs layer. Additional SEM images at 30 k × magnification and corresponding grain size statistics are provided in Fig. S4 and S5. Statistical analysis reveals a slight increase in average grain size from 244.92 nm to 276.44 nm upon A-GQDs modification. To understand the origin of the increased grain size after A-GQDs modification, we compared the XRD patterns of control and A-GQDs modified perovskite films (Fig. S6). The diffraction intensities of the (001), (002), and (012) planes are all substantially enhanced upon A-GQDs modification, indicating improved crystallinity. Together with the increase of grain size, the XRD evidence suggests that A-GQDs induce secondary grain growth. This phenomenon can be primarily attributed to the Ostwald ripening mechanism, which is well established in perovskite post-treatment studies.[33,34] Specifically, the polar IPA solvent and functional groups on A-GQDs, combined with the additional annealing step (100 °C), facilitates the dissolution of smaller, less thermodynamically stable grains and their re-deposition onto larger, more stable grains.[35] Collectively, the grain size enlargement arises from the interplay between thermal driving forces and chemical anchoring effects of A-GQDs.

Fourier-transform infrared (FT-IR) spectroscopy was employed to unravel the chemical interaction mechanisms at the molecular level. As shown in Fig. 2b and c, systematic shifts in characteristic vibrational peaks were observed when A-GQDs were respectively mixed with perovskite precursor components, PbI_2 and formamidinium iodide (FAI). In the A-GQDs + PbI_2 system, the pronounced red shifts of the N–H bending (-45.9 cm^{-1}) and C–O stretching (-41.1 cm^{-1}) peaks are characteristic of strong coordination interactions. Specifically, the lone-pair electrons on the amino nitrogen and hydroxyl oxygen atoms are donated to the empty 6p orbitals of Pb^{2+}, forming Pb–N and Pb–O bonds.[36] The smaller shift of the C–N stretching (-2.2 cm^{-1}) and C=O stretching (-9.4 cm^{-1})

suggests that while the amino group is involved in coordination, the C–N and C═O bonds are less directly affected. The broad N–H/O–H stretching peak also shifts to lower wavenumber (-18.4 cm^{-1}), further confirming the coordination mechanism. In the A-GQDs + FAI system, hydrogen bonding serves as the dominant interaction. The blue shift of N–H bending ($+8.9$ cm^{-1}) and red shift of N–H/O–H stretching (-23.5 cm^{-1}) stretching peaks are typical signature of the $-NH_2$ group acting as a hydrogen bond donor ($N–H\cdots I^-$).[37] The C–O (-92.5 cm^{-1}) and C–N (-65.1 cm^{-1}) stretching exhibit exceptionally large red shift comparing with C═O stretching (-0.2 cm^{-1}), indicating that the carbonyl oxygen and ammonia nitrogen serve as hydrogen bond acceptors ($C–O/N\cdots H–N$), interacting with the $-NH_2^+$/$-NH_3^+$ groups of FA^+/MA^+.[38] The direct FTIR comparison between pristine and A-GQDs-modified perovskite films further corroborates this interpretation (Fig. S7 and S8). The shifting peaks of N–H (3400.8 to 3395.6 cm^{-1}) and C–N (3264.4 to 3261.8 cm^{-1}) stretching vibrations of FA^+/MA^+ evidence hydrogen bonding ($C–O/N\cdots H–N$) between organic cations and A-GQDs. Most importantly, the Pb–I lattice stretching red shifts from 595.3 to 592.1 cm^{-1}, directly demonstrating Lewis-base groups ($-NH_2$, –OH and C═O) on A-GQDs donate lone-pair electrons to undercoordinated Pb^{2+}, forming coordination bonds (Pb–N, Pb–O) that reduce the Pb–I bond order and cause the characteristic red shift.[39] Collectively, these results demonstrate that a multimodal bonding configuration-comprising Pb–O/N coordination bonds alongside $N–H\cdots I^-$ and $C–O/N\cdots H–N$ hydrogen bonds-collectively establishes the chemical foundation for the robust anchoring of A-GQDs onto the perovskite surface.

X-ray photoelectron spectroscopy (XPS) depth profiling provides direct evidence for the aforementioned chemical interactions. As shown in Fig. 2d, compared to the pristine perovskite film, the Pb 4f characteristic peaks (Pb 4f 7/2 and Pb 4f 5/2) of A-GQDs-modified films exhibit a pronounced shift toward lower binding energies, from 138.47 eV and 143.36 eV to 137.17 eV and 142.02 eV, respectively. This decrease in binding energy signifies increased electron density around Pb atoms, directly attributable to successful coordination between electron-rich O/N atoms of A-GQDs and undercoordinated Pb^{2+} defect sites, with electron transfer from A-GQDs to Pb.[40] Similarly, as illustrated in Fig. 2e, the N 1s peaks associated with organic cations in the perovskite (corresponding to $-NH_2$ and $-NH_3^+$ of FA^+/MA^+, respectively) undergo distinct chemical shifts, further supporting the hydrogen bonding interactions between hydroxyl oxygen of A-GQDs and perovskite organic cations.[41] Moreover, the I 3d peaks shift from 619.4/630.9 eV to lower binding energies of 617.9/629.4 eV (Fig. 2f), consistent with the formation of $N–H\cdots I^-$ hydrogen bonds and the concomitant suppression of interfacial iodine vacancies.[42]

This synergistic passivation effect, wherein "coordination-dominated targeted defect healing" operates in concert with "hydrogen bonding-driven global stabilization", positions A-GQDs as a "versatile interfacial hub" within the perovskite interface architecture. This dual-modal chemical passivation mechanism, combined with the physical capping effect, collectively constructs an integral, stable, and defect-minimized upper perovskite interface. Based on the comprehensive analysis above, the schematic illustration of the synergistic multifunctional interaction mechanism of A-GQDs at the perovskite interface is proposed, as depicted in Fig. 2g.

2.3 Synergistic optimization of perovskite film by A-GQDs

To comprehensively evaluate the impact of A-GQDs interfacial modification on the intrinsic properties of the perovskite active layer, we systematically investigated the optical, electrical, and structural-mechanical characteristics of pristine and modified films. The photophysical properties were first examined following A-GQDs modification. As shown in Fig. S9, the modified films exhibit enhanced UV-vis absorption intensity across the 300–800 nm range, suggesting that the A-GQDs layer improves photon harvesting capability.[43] Photoluminescence (PL) measurements reveal effective defect passivation: the A-GQDs-modified films display significantly higher PL peak intensity compared to control films (Fig. S10a), directly indicating effective suppression of non-radiative recombination channels. This finding is further corroborated by the PL mapping spatial distributions presented in Fig. 3a and d, where modified films exhibit stronger and more uniform PL signals, demonstrating that the passivation effect of A-GQDs is macroscopically homogeneous. Time-resolved photoluminescence (TRPL) analysis provides quantitative evidence for carrier dynamics, as shown in Fig. S10b. The average carrier lifetime (τ_{ave}) of modified films is substantially prolonged from 286.72 ns to 671.59 ns (Table S2). This extended carrier lifetime unequivocally confirms that A-GQDs effectively reduce trap-assisted non-radiative recombination rates through defect passivation, facilitating the diffusion and collection of photogenerated carriers.

To elucidate the influence of the modification layer on local charge transport behavior and interfacial energy levels, conductive atomic force microscopy (C-AFM) and Kelvin probe force microscopy (KPFM) measurements were performed. C-AFM images (Fig. 3b) reveal that the pristine perovskite film exhibits inhomogeneous conductivity distribution with extensive dark regions (low current), corresponding to grain boundaries or areas with high defect density. In contrast, following A-GQDs modification (Fig. 3e), the current signal across the film surface is significantly enhanced and uniformly distributed, demonstrating that interfacial modification effectively promotes charge transport and reduces local electrical heterogeneity.[44] KPFM measurements of surface contact potential difference (CPD), presented in Fig. 3c, f, and S11, show that the surface potential of control films is -496 mV, which increases to -477 mV upon A-GQDs modification. This increase in CPD (decrease in absolute value) signifies a reduction in the work function of the film surface. Such energy level modulation is advantageous for lowering the electron extraction barrier between the perovskite and the upper electron transport layer (ETL), thereby enhancing charge separation and transport efficiency in the device.[45]

A fundamental requirement for flexible devices is the ability of the active layer to withstand sustained mechanical bending

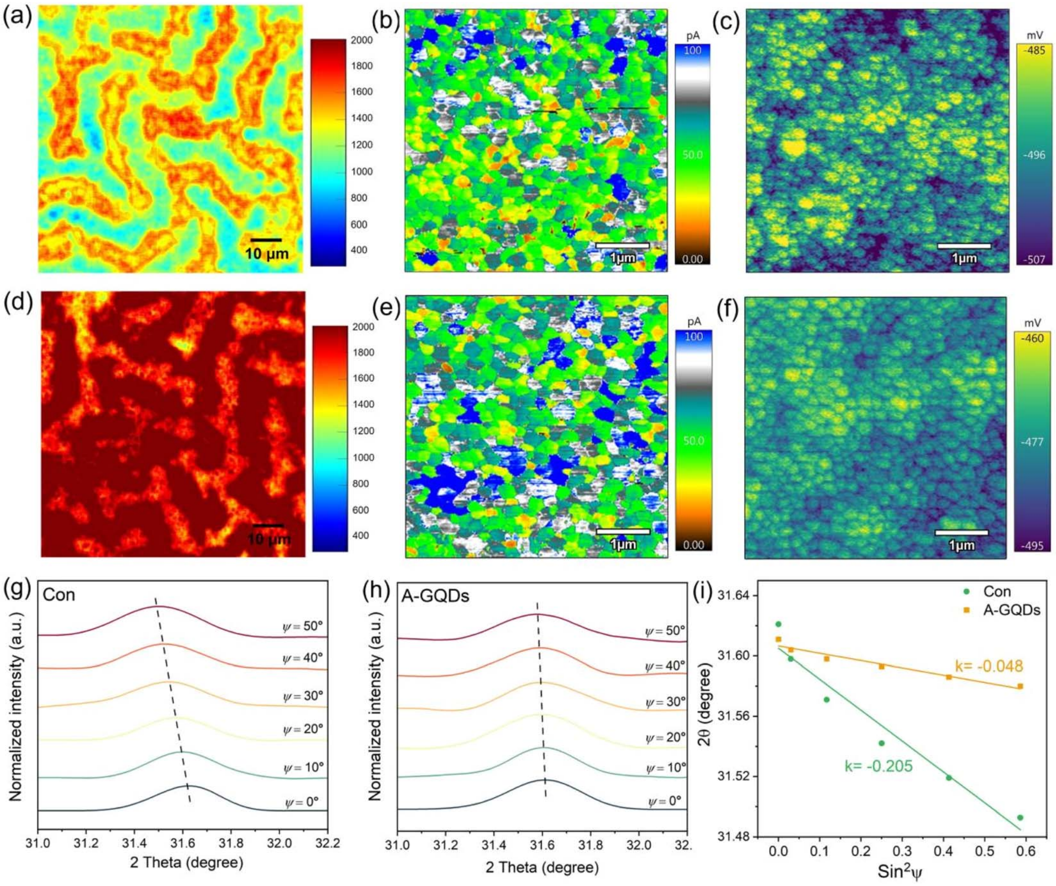

Fig. 3 PL mapping images of (a) control and (d) A-GQDs modified perovskite films. C-AFM current maps of control (b and e) A-GQDs modified perovskite films. KPFM images of (c) control and (f) A-GQDs modified perovskite films. GIXRD patterns with different instrumental diffraction ψ values (0°–50°) of (g) control and (h) A-GQDs modified perovskite films. (i) The corresponding linear fit of 2θ-$\sin^2\psi$.

stress. We employed multiple techniques to assess the improvement in film microstructure and mechanical properties conferred by A-GQDs. Atomic force microscopy (AFM) analysis (Fig. S12) reveals that the root mean square (RMS) surface roughness of modified films decreases substantially from 28.32 nm to 19.53 nm, indicating that A-GQDs fill surface voids and create a more planar interface. Furthermore, grazing-incidence X-ray diffraction (GIXRD) combined with the 2θ-$\sin^2\psi$ method was employed for in-depth analysis of residual film stress (Note S1). The (012) crystallographic plane ($2\theta \approx 31.6°$) was selected for stress analysis (Fig. 3g and h) due to its high diffraction angle and multiplicity factor, which provide the most reliable structural information.[46] Calculation results demonstrate that control films exhibit significant residual tensile stress reaching 48.52 GPa, whereas A-GQDs-modified films show a substantially reduced residual stress of 11.36 GPa (Fig. 3i). Additionally, the Young's modulus of A-GQDs-modified films decreases from 10.324 GPa to 5.528 GPa (Fig. S13). The A-GQDs layer thus functions as a "stress buffer", releasing strain between the perovskite and subsequent functional layers, thereby significantly enhancing the mechanical durability of flexible devices.[47]

2.4 A-GQDs modification enables high-efficiency FPSCs

Building upon the preceding demonstration that A-GQDs effectively passivate film defects, optimize photophysical properties, and enhance mechanical flexibility, this section integrates the modifier into complete FPSCs to systematically evaluate the impact of A-GQDs interfacial modification on device photovoltaic performance, charge carrier dynamics, and energy loss mechanisms. Fig. 4a presents the schematic illustration of the inverted FPSCs architecture employed in this study, with the specific configuration PET/ITO/NiO_x/MeO-4PACz/Perovskite/A-GQDs/PCBM/BCP/Ag.

To assess the effect of A-GQDs modification on device performance, control and A-GQDs-optimized devices were fabricated and characterized by current density–voltage (J–V) measurements. As shown in Fig. 4b, the control device achieves a PCE of 20.08%, with an open-circuit voltage (V_{oc}) of 1.104 V, short-circuit current density (J_{sc}) of 23.21 mA cm^{-2}, and fill factor (FF) of 78.37%, exhibiting pronounced hysteresis. In contrast, the A-GQDs-optimized device attains a champion PCE of 23.11% with substantially reduced hysteresis, accompanied by enhanced photovoltaic parameters: V_{oc} of 1.152 V, J_{sc} of 24.61 mA cm^{-2}, and FF of 81.52% (Table S3). Systematic optimization of A-GQDs concentration in isopropanol (0, 0.5, 1.0, and 1.5 mg

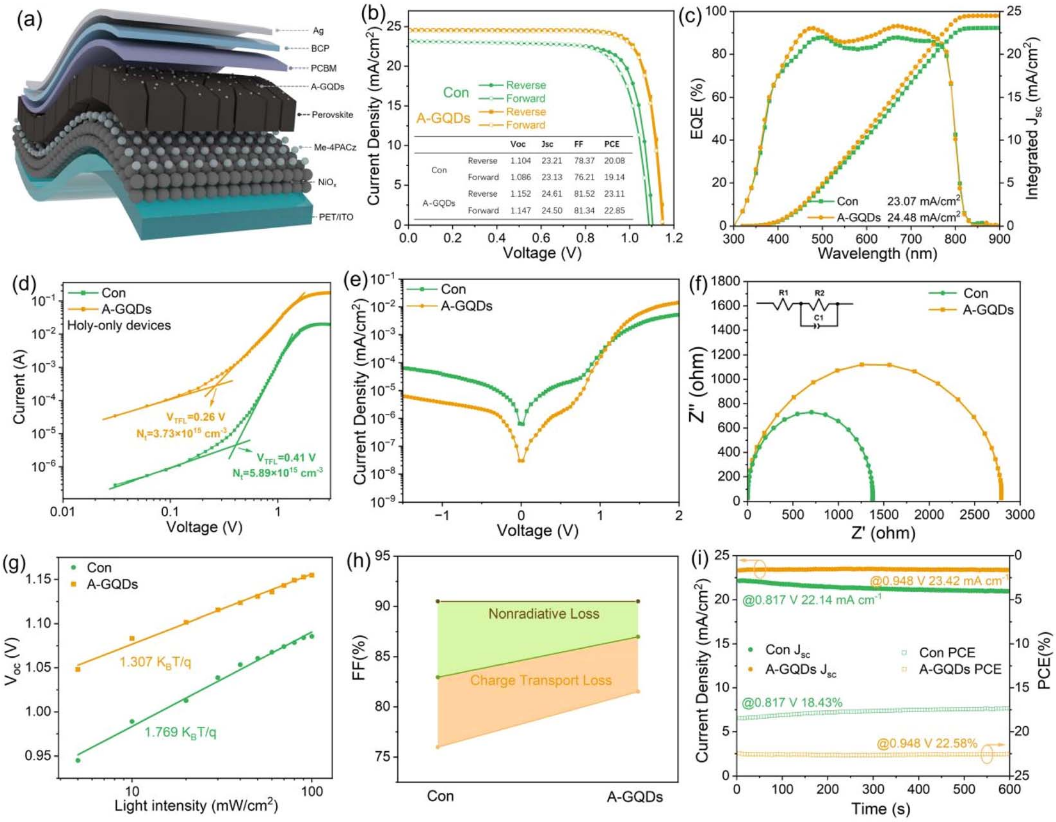

		Voc	Jsc	FF	PCE
Con	Reverse	1.104	23.21	78.37	20.08
	Forward	1.086	23.13	76.21	19.14
A-GQDs	Reverse	1.152	24.61	81.52	23.11
	Forward	1.147	24.50	81.34	22.85

Fig. 4 (a) Schematic illustration of the FPSCs. (b) *J*–*V* curves of both reverse and forward scans of control and A-GQDs optimized FPSCs. (c) EQE spectra and integrated J_{SC} curves of control and A-GQDs optimized FPSCs. (d) The holy-only SCLC curves of control and A-GQDs modified FPSCs. (e) Dark *J*–*V* curves of control and A-GQDs modified FPSCs. (f) Nyquist plots of the control and A-GQDs optimized FPSCs. (g) Light intensity dependence of V_{oc}. (h) FF Shockley–Queisser (S–Q) limit diagram of the device (brown, green and orange spheres correspond to FF_{S-Q}, FF_{max} and measured FF respectively; green areas correspond to non-radiation loss; orange areas correspond to charge transfer loss). (i) Stabilized photocurrent outputs and PCEs, corresponding to the MPP tracking.

mL^{-1}) identifies 1.0 mg mL^{-1} as the optimal concentration (Fig. S14). To demonstrate the scale-up potential of A-GQDs in FPSCs, we fabricated large-area flexible perovskite solar modules with a substrate size of 5 cm × 5 cm (active areas about 10.45 cm^2). As shown in Fig. S15 and Table S4, the champion A-GQDs-optimized module achieved the PCE of 20.24%, with V_{oc} of 6.466 V, J_{sc} of 4.09 mA cm^{-2}, and FF of 76.56. In contrast, the control module (without A-GQDs) delivered the PCE of 18.02%. Notably, the A-GQDs modified module exhibited substantially reduced hysteresis between forward and reverse scans, indicating that interface modification effectively suppresses ion migration and charge trapping in large-area perovskite films.

External quantum efficiency (EQE) spectra and corresponding integrated current densities are presented in Fig. 4c. The A-GQDs-modified device exhibits enhanced EQE response across the entire spectral range, with particularly pronounced improvement in the 400–750 nm region. The integrated current density increases from 23.07 mA cm^{-2} for the control device to 24.48 mA cm^{-2} for the optimized device, showing excellent agreement with *J*–*V* measurements. Differentiation of the EQE spectrum for the optimized device (Fig. S16) confirms an optical bandgap of 1.55 eV for the perovskite absorber, consistent with expectations.[48] To elucidate the underlying electrical mechanisms responsible for the enhanced photovoltaic performance upon A-GQDs modification, the trap-state density within perovskite films was first evaluated by space-charge-limited current (SCLC) method. Hole-only devices with the structure ITO/NiO_x/Perovskite/Spiro-OMeTAD/Ag were fabricated and characterized, as shown in Fig. 4d. The trap-filled limit voltage (V_{TFL}) extracted from the dark *J*–*V* curves was employed to calculate the trap-state density according to Note S2. The control device exhibits a V_{TFL} of 0.41 V, corresponding to a trap-state density of 5.89 × 10^{15} cm^{-3}, whereas the optimized device displays a reduced V_{TFL} of 0.26 V, corresponding to a diminished trap-state density of 3.73 × 10^{15} cm^{-3}. Fig. 4e presents the dark *J*–*V* characteristics and corresponding Tafel plots for both devices. The optimized device exhibits substantially lower dark current density near zero bias compared to the control, indicating effective suppression of leakage current pathways and enhanced shunt resistance.[49] Electrochemical impedance spectroscopy (EIS) measurements (Fig. 4f) further corroborate these findings, revealing that the optimized device possesses significantly higher recombination resistance (R_{rec}), demonstrating effective suppression of interfacial non-radiative recombination processes and enabling more efficient separation and extraction of photogenerated carriers.[50]

To gain deeper insight into the carrier recombination mechanisms within the devices, the dependence of V_{oc} on light intensity (I) was investigated (Fig. 4g). According to the relationship of $V_{oc} \propto (nkT/q)\ln(I)$, the fitted slope provides information on the dominant recombination kinetics.[51] The control device exhibits a slope of 1.769 kT/q, substantially deviating from the ideal value of unity, indicating pronounced trap-assisted Shockley-Read-Hall (SRH) recombination. Remarkably, the optimized device displays a reduced slope of 1.307 kT/q, approaching the ideal value and confirming that A-GQDs modification effectively suppresses trap-dominated SRH recombination. This finding is in excellent agreement with the conclusions drawn from SCLC, EIS, and steady-state/transient PL measurements. Quantitative analysis of FF losses based on the Shockley–Queisser (S–Q) limit theory is presented in Fig. 4h and Note S3. The A-GQDs-optimized device exhibits reduced non-radiative recombination losses and diminished charge transport losses compared to the control, consistent with the observed enhancement in both V_{oc} and FF.

To further elucidate the origins of V_{oc} and FF enhancement, ultraviolet photoelectron spectroscopy (UPS) measurements were performed (Fig. S17). The calculated work function (W_F) of the pristine perovskite film is approximately 5.30 eV, which decreases to 4.84 eV upon A-GQDs modification (Note S4), showing excellent agreement with the increased surface potential (reduced work function) observed in KPFM measurements. Based on these findings, energy level alignment diagrams between the perovskite and PCBM electron transport layer were constructed before and after modification (Fig. S18). The relatively high work function of the pristine perovskite results in a substantial energy mismatch between its conduction band minimum and the LUMO level of PCBM, creating an electron extraction barrier. Following A-GQDs modification, the reduced perovskite work function induces an upward shift of the conduction band, transforming the energy level alignment from an unfavorable "cliff-like" configuration to a more desirable "staircase-like" configuration. This optimized alignment substantially reduces the interfacial energy barrier, facilitating efficient electron extraction (Fig. S19). Photogenerated electrons can thus transfer more readily from the perovskite conduction band into PCBM, minimizing interfacial accumulation and recombination losses. This energy level optimization mechanism constitutes a fundamental origin of the concurrently enhanced V_{oc} and FF in A-GQDs-modified devices.[52]

Beyond investigating the efficiency enhancement mechanisms conferred by A-GQDs, the operational stability of devices under continuous MPP tracking for 600 s was evaluated (Fig. 4i). In contrast to the control device, the A-GQDs-optimized device exhibits superior output stability throughout the testing period. This enhanced operational robustness correlates closely with the defect passivation, interfacial energy level optimization, and residual stress relief demonstrated in preceding sections, collectively confirming that A-GQDs modification substantially improves the durability of flexible devices under sustained operation.

2.5 Stability enhancement of FPSCs by A-GQDs

Operational stability remains one of the most critical bottlenecks impeding the practical deployment of FPSCs. This section systematically evaluates the impact of A-GQDs modification on the durability of both perovskite films and complete FPSCs under various aging conditions.

Ion migration, particularly the diffusion of I^- toward the metal electrode and the reverse infiltration of Ag^+ into the perovskite layer, constitutes a key mechanism underlying the performance degradation of FPSCs. To investigate the inhibitory effect of A-GQDs modification on ion migration, time-of-flight secondary ion mass spectrometry (TOF-SIMS) depth profiling was performed on complete devices after photothermal aging (100 h). In the control device, I^- ions are distributed not only within the perovskite layer but also exhibit strong signals in the near-surface region adjacent to the Ag electrode, indicating substantial diffusion of I^- to the device surface. Simultaneously, Ag^+ signals are abundantly present throughout the perovskite depth profile, demonstrating backward diffusion of silver electrode metal ions into the perovskite active layer (Fig. 5a and c). The A-GQDs-optimized device presents a markedly different distribution profile: I^- signals are effectively confined within the perovskite layer with significantly reduced intensity at the surface, while the diffusion depth and intensity of Ag^+ into the perovskite layer are substantially suppressed (Fig. 5b and d). Furthermore, the Ag^+ surface 2D mapping images (Fig. S20) reveal that the control device exhibits low-intensity, non-uniform Ag^+ signals on the surface, likely attributable to the formation of AgI clusters *via* reaction between diffused Ag^+ and I^-.[53] In contrast, the optimized device displays higher intensity and more uniform Ag^+ signals, indicating preservation of the Ag electrode integrity and effective suppression of interfacial reactions. These TOF-SIMS results provide direct evidence that the A-GQDs modification layer functions as a critical "ion diffusion barrier" during device operation. The multimodal chemical bonding network formed between A-GQDs and the perovskite effectively anchors susceptible mobile ions, thereby significantly enhancing device operational stability.

To intuitively assess the impact of A-GQDs on the photothermal stability of perovskite films, control and A-GQDs-modified films were subjected to accelerated aging under coupled stress conditions comprising 1 sun illumination (AM 1.5 G) and 85 °C for up to 720 hours, with morphological evolution monitored *in situ* by SEM. As shown in Fig. S21, the control film exhibits localized degradation signatures at the early aging stage (24 h), with the film surface rapidly becoming covered by numerous block-like crystals as aging progresses. Based on XRD results (detailed below), these crystals are identified as lead iodide (PbI_2), the degradation product. By 720 h, the control film is completely eroded by PbI_2, with the original perovskite grain morphology becoming virtually unrecognizable. In striking contrast, the A-GQDs-modified film demonstrates exceptional morphological stability throughout the entire aging process (Fig. S22). Although a few pinholes gradually emerge on the film surface over time, the grain structure

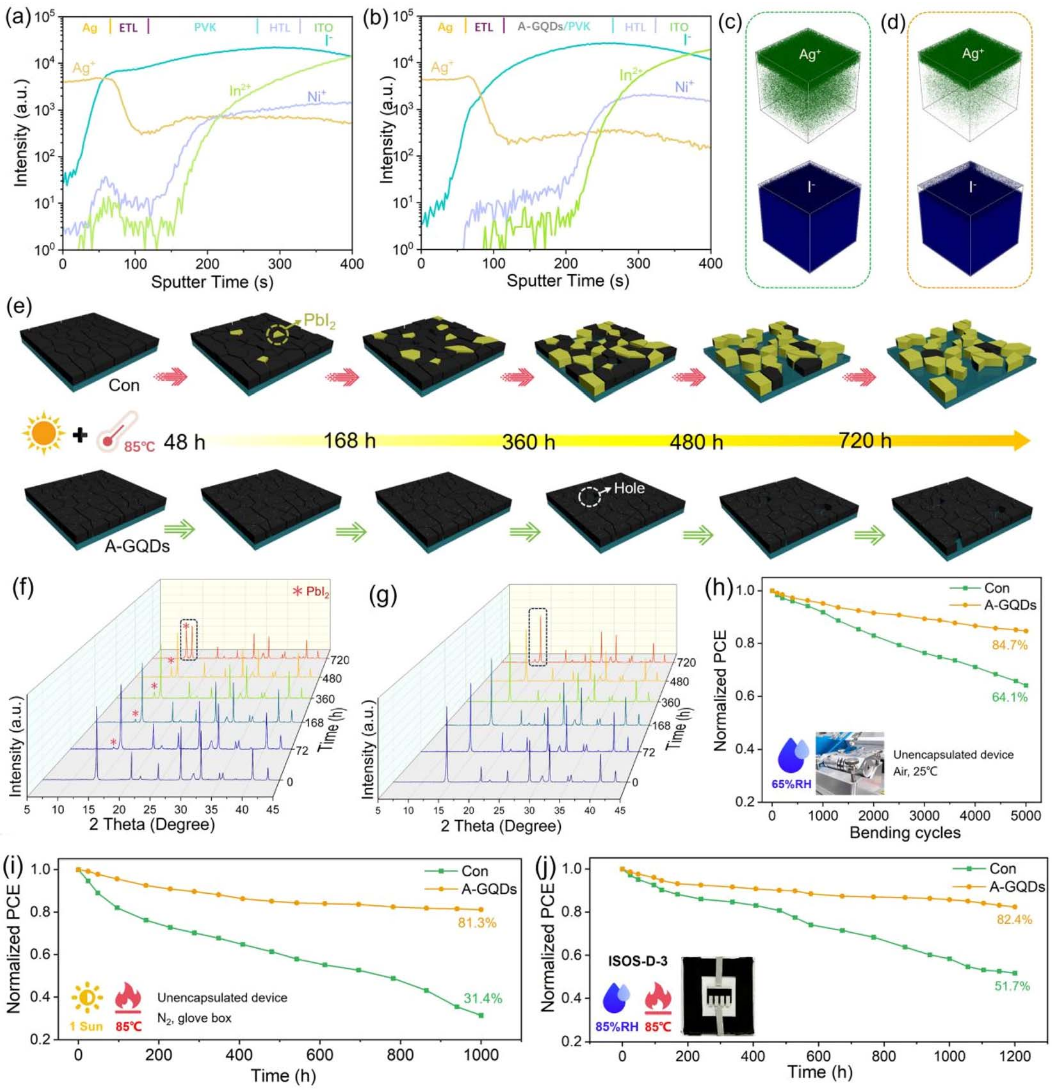

Fig. 5 Depth profiles of TOF-SIMS for aged (a) control and (b) A-GQDs modified devices, aging at 1-sun illumination and 85 °C heating for 100 hours in N_2. Volume distribution of Ag^+ and I^- of (c) control and (d) A-GQDs modified devices. (e) Aging schematic diagram of control perovskite films at different times from 0 h to 720 h under continuous 1-sun illumination and 85 °C heating corresponding to SEM aging measurement. XRD aging spectrum of (f) control and (g) A-GQDs modified perovskite films under 1-sun illumination and 85 °C heating. (h) The mechanical stability of unencapsulated FPSCs at a 10 mm bending radius in air. (i) Operational stability of unencapsulated FPSCs under 1-sun illumination and 85 °C heating in N_2. (j) Stability testing of encapsulated FPSCs in the dark at 85 °C and 85% RH.

remains intact up to 720 h, with no observable PbI_2 crystal precipitation. This comparison provides compelling evidence that the A-GQDs modification layer effectively suppresses photothermal stress-induced perovskite decomposition. Based on these observations, a schematic mechanism illustrating A-GQDs inhibition of perovskite photothermal degradation is presented in Fig. 5e.

X-ray diffraction (XRD) analysis provides quantitative crystallographic evidence corroborating the morphological observations. The evolution of XRD patterns for control and A-GQDs-modified films during photothermal aging are presented in Fig. 5f and g, respectively. For the control film (Fig. 5f), the intensity of the (001) principal diffraction peak progressively attenuates with aging time, while the PbI_2 characteristic peak at 12.8° rapidly intensifies. By 720 h, the PbI_2 peak intensity becomes comparable to that of the perovskite, indicating severe film decomposition. In contrast, although the (001) peak intensity of the A-GQDs-modified film also decreases with aging time, the rate is markedly slower (Fig. 5g). The PbI_2 characteristic exhibits only negligible growth throughout the entire aging process, with intensity substantially lower than that of the control film. These results directly confirm that A-GQDs modification effectively suppresses perovskite lattice decomposition under photothermal stress, retarding PbI_2 generation and accumulation, thereby ensuring long-term structural stability of the film at its source. Additionally, the influence of A-GQDs modification on the surface hydrophilicity/hydrophobicity of perovskite films was evaluated (Fig. S23). A-GQDs modification increases the water contact angle from 53.30° to 81.74°, rendering the surface more hydrophobic. The more hydrophobic surface contributes to prevent ambient moisture from penetrating into the perovskite layer, thereby enhancing the moisture stability of the device.

The operational stability of complete FPSCs devices under various stress conditions was systematically evaluated. Mechanical bending stability, a core requirement for flexible devices, was assessed by subjecting FPSCs to repeated bending at a 10 mm radius under 65% relative humidity (Fig. 5h). The control device retains only 64.1% of its initial efficiency after 5000 bending cycles, whereas the A-GQDs-optimized device maintains 84.7% of its original efficiency. This enhanced bending durability correlates closely with the mechanical optimization effects conferred by A-GQDs, including residual stress relief and reduced Young's modulus demonstrated in preceding sections. Photothermal coupling stability, critical for assessing device practicality, was evaluated by tracking device performance under continuous 1 sun illumination combined with 85 °C heating (Fig. 5i). The control device exhibits rapid performance decay, retaining only 31.4% of its initial efficiency after 1000 h. Remarkably, the A-GQDs-optimized device demonstrates exceptional photothermal tolerance, maintaining 81.3% of its initial efficiency after 1000 h. This result aligns closely with the ion migration suppression effects revealed by TOF-SIMS and the inhibited PbI_2 formation evidenced by SEM and XRD, confirming that A-GQDs effectively suppress photothermal-induced degradation reactions. Damp heat stability, simulating extreme environmental conditions that photovoltaic modules may encounter during outdoor operation, was investigated by aging encapsulated devices in a constant temperature-humidity chamber at 85% relative humidity and 85 °C (Fig. 5j). The control device undergoes continuous performance degradation, retaining only 51.7% of its initial efficiency after 1200 h. In contrast, the optimized device maintains 82.4% of its initial efficiency under identical aging conditions. The synergistic effect of the hydrophobic surface and the barrier against moisture/oxygen ingress substantially delays interface degradation induced by humidity. Furthermore, unencapsulated devices were directly exposed to ambient air at 65% relative humidity for storage stability assessment (Fig. S24). The control device retains only 40.2% of its initial efficiency after 1400 h, while the A-GQDs-optimized device exhibits superior storage stability, maintaining 83.6% of its initial efficiency over the same period.

3. Conclusions

This study addresses the critical challenge of upper interface instability in FPSCs under photothermal stress, which triggers detrimental PbI_2 formation and accelerates performance degradation. A-GQDs are innovatively proposed and systematically validated as an effective multifunctional interface modifier. The A-GQDs layer transcends conventional static passivation, exhibiting sustained passivation and stress-buffering capabilities that suppress PbI_2 accumulation, block ion migration, release residual stress, and enhance mechanical flexibility. A-GQDs-modified F-PSCs achieve 23.11% efficiency with minimal hysteresis, retaining 81.3% of initial performance after 1000 h photothermal aging (*versus* 31.4% for control), along with superior bending, damp heat, and storage stability. By synergistically enabling defect passivation, energy alignment, ion blocking, degradation suppression, and stress relief, this work provides a novel pathway toward resolving the efficiency-stability dilemma in flexible perovskite photovoltaics.

Conflicts of interest

The authors declare no conflict of interest.

Data availability

The data that support the findings of this study are available from the corresponding author upon reasonable request.

Supplementary information (SI) is available. See DOI: https://doi.org/10.1039/d6ta02867e.

Acknowledgements

This work was supported by the National Natural Science Foundation of China (No. 62175204) and the National Key R&D Program of China (No. 2022YFE0118400).

References

1 J. Han, K. Park, S. Tan, Y. Vaynzof, J. Xue, E. W.-G. Diau, M. G. Bawendi, J.-W. Lee and I. Jeon, Perovskite solar cells, *Nat. Rev. Methods Primers*, 2025, **5**, 3.
2 H. S. Jung, G. S. Han, N.-G. Park and M. J. Ko, Flexible Perovskite Solar Cells, *Joule*, 2019, **3**, 1850–1880.
3 H. Wang and X. Li, In-Situ Polymerization Strategies for Flexible Perovskite Solar Cells: Mechanisms and Prospects, *Adv. Mater. Technol.*, 2025, **10**, 2401606.
4 S. Wang, W. Li, C. Yu, W. Shi, Q. Kang, F. Cao, K. Gao, L. Yang, B. Yang, J. Zhou, S. Yang, Q. Wang, Q. Fei, X. Chen, G. Chen, P. Chen, Z. Li, W.-C. Hsu, Z. Yan, Y. Bai, W. Liu, S. De Wolf, X. Yang and X. Zhang, Flexible perovskite/silicon tandem solar cells with 33.6% efficiency, *Nature*, 2026, **649**, 59–64.
5 Z. Xu, R. Yu, Q. Lv, H. Jia, Q. Guo, T. Xue, R. Wang, H. Gao, E. Zhou and Z. A. Tan, Tensile strain regulation via grain boundary buffering for flexible perovskite solar cells, *Nat. Commun.*, 2025, **17**, 322.
6 Y. Li, Y. Wang, Z. Xu, B. Peng and X. Li, Key Roles of Interfaces in Inverted Metal-Halide Perovskite Solar Cells, *ACS Nano*, 2024, **18**, 10688–10725.
7 X. Zhang, S. Wu, H. Zhang, A. K. Y. Jen, Y. Zhan and J. Chu, Advances in inverted perovskite solar cells, *Nat. Photonics*, 2024, **18**, 1243–1253.
8 H. Wang, C. Liu, R. Xu, Y. Zhang, S. De Wolf and K. Wang, Upper Interface Engineering Between Perovskite and Electron Transport Layer Toward Efficient and Stable Inverted Perovskite Solar Cells, *Adv. Mater.*, 2026, **38**, e13633.

9 J. Wang, Y. Wu, J. Zhao, S. Lu, J. Lu, J. Sun, S. Wu, X. Zheng, X. Zheng, X. Tang, M. Ma, S. Yue, K. Liu, Z. Wang and S. Qu, Unraveling the Molecular Size Effect on Surface Engineering of Perovskite Solar Cells, *Small Methods*, 2024, **8**, 2400043.

10 X. Huo, S. Mariotti, Y. Li, T. Guo, C. Ding, P. Ji, S. Yuan, T. Li, N. Meng, X. Liu, J. Zhang, I. N. Rabehi, Y. Zhang, S. Zhao, H. Wang, D. Song, L. K. Ono, Z. Xu and Y. Qi, Unraveling the relationship between the phenethylammonium-induced 2D phase on the perovskite surface and inverted wide bandgap perovskite solar cell performance, *Energy Environ. Sci.*, 2024, **17**, 8658–8669.

11 Z. Dai, Y. Yang, X. Huang, S. Wan, L. Yuan, H. Wei, S. Nie, Z. Liu, Y. Wu, R. Chen and H. Wang, Interfacial crosslinking benzimidazolium enables eco-friendly inverted perovskite solar cells and modules, *Nano Energy*, 2024, **131**, 110190.

12 Z. Xing, S. Ma, B.-W. Chen, M. An, A. Fan, X. Hu, Y. Wang, L.-L. Deng, Q. Huang, H. Kanda, F. G. Al-Amri, G. Pozzi, Y. Zhang, J. Xia, J. Wu, X. Guo and M. K. Nazeeruddin, Solubilizing and stabilizing C60 with n-type polymer enables efficient inverted perovskite solar cells, *Joule*, 2025, **9**, 101817.

13 K. Artuk, D. Turkay, M. D. Mensi, J. A. Steele, D. A. Jacobs, M. Othman, X. Yu Chin, S.-J. Moon, A. N. Tiwari, A. Hessler-Wyser, Q. Jeangros, C. Ballif and C. M. Wolff, A Universal Perovskite/C60 Interface Modification via Atomic Layer Deposited Aluminum Oxide for Perovskite Solar Cells and Perovskite–Silicon Tandems, *Adv. Mater.*, 2024, **36**, 2311745.

14 Y.-h. Li, X.-x. Feng, M.-q. Long, M.-q. Cai, J.-l. Yang and B. Liu, Interface engineering of $FAPbI_3$ for passivating defects and improving stability with lead chalcogenides, *J. Cent. S. Univ.*, 2024, **31**, 4625–4637.

15 V. S. N. Chava, P. S. Chandrasekhar, A. Gomez, L. Echegoyen and S. T. Sreenivasan, MXene-Based Tailoring of Carrier Dynamics, Defect Passivation, and Interfacial Band Alignment for Efficient Planar p–i–n Perovskite Solar Cells, *ACS Appl. Energy Mater.*, 2021, **4**, 12137–12148.

16 J. Xing, C. Liu, Q. Cao, F. Xie, X. Zeng, X. Zhang and H. Liu, Molecular-Perspective Insights into Top Interface Passivation in Inverted Perovskite Solar Cells, *Small*, 2025, **21**, e06495.

17 N. Ahn and M. Choi, Towards Long-Term Stable Perovskite Solar Cells: Degradation Mechanisms and Stabilization Techniques, *Advanced Science*, 2024, **11**, 2306110.

18 J. Wei, Q. Wang, J. Huo, F. Gao, Z. Gan, Q. Zhao and H. Li, Mechanisms and Suppression of Photoinduced Degradation in Perovskite Solar Cells, *Adv. Energy Mater.*, 2021, **11**, 2002326.

19 Z. Wang, Z. Zhang, L. Xie, S. Wang, C. Yang, C. Fang and F. Hao, Recent Advances and Perspectives of Photostability for Halide Perovskite Solar Cells, *Adv. Opt. Mater.*, 2022, **10**, 2101822.

20 H. Wang, Q. Li, Y. Zhu, X. Sui, X. Fan, M. Lin, Y. Shi, Y. Zheng, H. Yuan, Y. Zhou, H. Jin, H. G. Yang, Y. Hou and S. Yang, Photomechanically accelerated degradation of perovskite solar cells, *Energy Environ. Sci.*, 2025, **18**, 2254–2263.

21 J. Xie, K. Huang, X. Yu, Z. Yang, K. Xiao, Y. Qiang, X. Zhu, L. Xu, P. Wang, C. Cui and D. Yang, Enhanced Electronic Properties of SnO_2 via Electron Transfer from Graphene Quantum Dots for Efficient Perovskite Solar Cells, *ACS Nano*, 2017, **11**, 9176–9182.

22 S. Pang, C. Zhang, H. Zhang, H. Dong, D. Chen, W. Zhu, H. Xi, J. Chang, Z. Lin, J. Zhang and Y. Hao, Boosting performance of perovskite solar cells with Graphene quantum dots decorated SnO_2 electron transport layers, *Appl. Surf. Sci.*, 2020, **507**, 145099.

23 Z.-W. Gao, Y. Wang, H. Liu, J. Sun, J. Kim, Y. Li, B. Xu and W. C. H. Choy, Tailoring the Interface in $FAPbI_3$ Planar Perovskite Solar Cells by Imidazole-Graphene- Quantum-Dots, *Adv. Funct. Mater.*, 2021, **31**, 2101438.

24 Y. Zhou, S. Yang, X. Yin, J. Han, M. Tai, X. Zhao, H. Chen, Y. Gu, N. Wang and H. Lin, Enhancing electron transport via graphene quantum dot/SnO_2 composites for efficient and durable flexible perovskite photovoltaics, *J. Mater. Chem. A*, 2019, **7**, 1878–1888.

25 Q. Hu, K. Zhao, M. Liu, S. Riaz, Y. Qi, P. Wei, J. Cheng and Y. Xie, A dual passivation strategy based on F/N co-doped coal-based graphene quantum dots for high-efficiency carbon-based perovskite solar cells, *J. Mater. Chem. A*, 2024, **12**, 5980–5989.

26 Y. Chen, J. Chen, X. Wang, P. Deng, Y. Shen and X. Wang, Fluorinated graphene quantum dots-induced defect passivation of perovskite film toward stable and efficient perovskite solar cell, *Int. J. Hydrogen Energy*, 2025, **137**, 107–113.

27 L. Yang, Y. Li, L. Wang, Y. Pei, Z. Wang, Y. Zhang, H. Lin and X. Li, Exfoliated Fluorographene Quantum Dots as Outstanding Passivants for Improved Flexible Perovskite Solar Cells, *ACS Appl. Mater. Interfaces*, 2020, **12**, 22992–23001.

28 S. H. Shin, D. H. Shin and S.-H. Choi, Enhancement of Stability of Inverted Flexible Perovskite Solar Cells by Employing Graphene-Quantum-Dots Hole Transport Layer and Graphene Transparent Electrode Codoped with Gold Nanoparticles and Bis(trifluoromethanesulfonyl)amide, *ACS Sustain. Chem. Eng.*, 2019, **7**, 13178–13185.

29 F. Khan, M. T. Khan, S. Rehman and F. Al-Sulaiman, Analysis of electrical parameters of p-i-n perovskites solar cells during passivation via N-doped graphene quantum dots, *Surf. Interfaces*, 2022, **31**, 102066.

30 X. Gan, S. Yang, J. Zhang, G. Wang, P. He, H. Sun, H. Yuan, L. Yu, G. Ding and Y. Zhu, Graphite-N Doped Graphene Quantum Dots as Semiconductor Additive in Perovskite Solar Cells, *ACS Appl. Mater. Interfaces*, 2019, **11**, 37796–37803.

31 Z.-W. Gao, Y. Wang, H. Liu, J. Sun, J. Kim, Y. Li, B. Xu and W. C. H. Choy, Tailoring the Interface in $FAPbI_3$ Planar Perovskite Solar Cells by Imidazole-Graphene-Quantum-Dots, *Adv. Funct. Mater.*, 2021, **31**, 2101438.

32 C. Ren, C. Tian, W. Cao, M. Zhang, T. Zhang, J. Tang, F. Zhang, G. Chen and J. Tang, Controllable

functionalization of amino-functionalized graphene quantum dots as fluorescent probe for detection of Cu(II) ions detection, *Mater. Lett.*, 2024, **364**, 136393.

33 N. D. Pham, V. T. Tiong, D. Yao, W. Martens, A. Guerrero, J. Bisquert and H. Wang, Guanidinium thiocyanate selective Ostwald ripening induced large grain for high performance perovskite solar cells, *Nano Energy*, 2017, **41**, 476–487.

34 Z. Liu, C. Zhu, H. Luo, W. Kong, X. Luo, J. Wu, C. Ding, Y. Chen, Y. Wang, J. Wen, Y. Gao and H. Tan, Grain Regrowth and Bifacial Passivation for High-Efficiency Wide-Bandgap Perovskite Solar Cells, *Adv. Energy Mater.*, 2023, **13**, 2203230.

35 M. Yang, T. Zhang, P. Schulz, Z. Li, G. Li, D. H. Kim, N. Guo, J. J. Berry, K. Zhu and Y. Zhao, Facile fabrication of large-grain $CH_3NH_3PbI_{3-x}Br_x$ films for high-efficiency solar cells via CH_3NH_3Br-selective Ostwald ripening, *Nat. Commun.*, 2016, **7**, 12305.

36 X. Chen, L. Ai, H. Ji and W. Song, Silane Doping for Efficient Flexible Perovskite Solar Cells with Improved Defect Passivation and Device Stability, *ACS Appl. Mater. Interfaces*, 2024, **16**, 23668–23676.

37 L. Lin, T. W. Jones, T. C.-J. Yang, X. Li, C. Wu, Z. Xiao, H. Li, J. Li, J. Qian, L. Lin, J. Q. Shi, S. D. Stranks, G. J. Wilson and X. Wang, Hydrogen bonding in perovskite solar cells, *Matter*, 2024, **7**, 38–58.

38 B. Zhang, M. Li, L. Li, W. Zhang, Y. Song and Z. Wang, Multifunctional Interfacial Passivation via Cooperative Coordination and Hydrogen Bonding for Highly Efficient and Stable Inverted Perovskite Solar Cells, *Adv. Funct. Mater.*, 2026, e75040.

39 J. Nishida, J. P. Breen, K. P. Lindquist, D. Umeyama, H. I. Karunadasa and M. D. Fayer, Dynamically Disordered Lattice in a Layered Pb-I-SCN Perovskite Thin Film Probed by Two-Dimensional Infrared Spectroscopy, *J. Am. Chem. Soc.*, 2018, **140**, 9882–9890.

40 J. Wang, X.-Y. Dai, L. Bi, J. Sun, M. Liu, X. Ji, F. R. Lin, Q. Fu and A. K. Y. Jen, Synergistic iodine and lead chelation with redox cycling via supramolecular engineering for stable and sustainable perovskite solar cells, *Joule*, 2025, **9**, 102105.

41 X. Feng, M. Tan, M. Li, H. Wei and B. Yang, Polyhydroxy Ester Stabilized Perovskite for Low Noise and Large Linear Dynamic Range of Self-Powered Photodetectors, *Nano Lett.*, 2021, **21**, 1500–1507.

42 S. Xiong, F. Tian, F. Wang, A. Cao, Z. Chen, S. Jiang, D. Li, B. Xu, H. Wu, Y. Zhang, H. Qiao, Z. Ma, J. Tang, H. Zhu, Y. Yao, X. Liu, L. Zhang, Z. Sun, M. Fahlman, J. Chu, F. Gao and Q. Bao, Reducing nonradiative recombination for highly efficient inverted perovskite solar cells via a synergistic bimolecular interface, *Nat. Commun.*, 2024, **15**, 5607.

43 J. Yang, J. Wang, Y. Xie, H. Xu, M. Duan, T. Li, J. Wen, C. Zhang, Y. Xia, H. Zhang and Y. Chen, Environmentally Friendly Flexible Perovskite Solar Cells with Promoted Thermal Diffusivity and Suppressed Lead Leakage, *Adv. Energy Mater.*, 2025, **15**, e01673.

44 X. Chang, Y. Liu, Y. Ping, N. Wu, T. Yang, C. Tian, Z. Ling, B. Vishal, A. R. Pininti, J. B. Park, S. Y. Jeong, Y. Qin, W. T. Hui, F. S. Y. Yeung, Y.-Y. Yang, H. Liao, A. Prasetio, F. H. Isikgor, M. He, D. S. Utomo, R. Wang, K. Zhao, M. Lanza, H. Y. Woo, M. Heeney, S. De Wolf, Y.-H. Lin, L. Tsetseris, R. Azmi and T. D. Anthopoulos, Multivalent ligands regulate dimensional engineering for inverted perovskite solar modules, *Science*, 2026, **391**, 153–159.

45 Z. Lan, H. Huang, Y. Lu, S. Qu, M. Wang, S. Du, Y. Yang, C. Sun, Q. Zhang, Y. Suo, X. Wang, L. Yan, P. Cui, Z. Zhao and M. Li, Homogenizing the Electron Extraction via Eliminating Low-Conductive Contacts Enables Efficient Perovskite Solar Cells with Reduced Up-Scaling Losses, *Adv. Funct. Mater.*, 2024, **34**, 2316591.

46 Z. Zheng, F. Li, J. Gong, Y. Ma, J. Gu, X. Liu, S. Chen and M. Liu, Pre-Buried Additive for Cross-Layer Modification in Flexible Perovskite Solar Cells with Efficiency Exceeding 22%, *Adv. Mater.*, 2022, **34**, 2109879.

47 S. Tu, Y. Gang, Y. Lin, X. Liu, Y. Zhong, D. Yu and X. Li, Triple Cross-Linking Engineering Strategies for Efficient and Stable Inverted Flexible Perovskite Solar Cells, *Small*, 2024, **20**, 2310868.

48 S. Tu, W. Chen, Y. Gang, Q. Xiong and X. Li, Engineering a thermally robust hole-selective layer for stable flexible perovskite solar cells, *Chem. Eng. J.*, 2025, **503**, 158389.

49 P. Liao, X. Zhao, G. Li, Y. Shen and M. Wang, A New Method for Fitting Current–Voltage Curves of Planar Heterojunction Perovskite Solar Cells, *Nano-Micro Lett.*, 2017, **10**, 5.

50 B. Roose, K. Dey, M. R. Fitzsimmons, Y.-H. Chiang, P. J. Cameron and S. D. Stranks, Electrochemical Impedance Spectroscopy of All-Perovskite Tandem Solar Cells, *ACS Energy Lett.*, 2024, **9**, 442–453.

51 H. Zhao, J. Ding, X. Liu, D. He, Y. Yu, J. Yi, C. Chen, J. Hou and J. Chen, Intermolecular Interaction Induced Synergistic Uniform Passivation of Grain Boundary Multiple Defects Enables High-Performance Inverted Perovskite Solar Cells, *Adv. Funct. Mater.*, 2025, 2504424.

52 Z. Li, X. Sun, X. Zheng, B. Li, D. Gao, S. Zhang, X. Wu, S. Li, J. Gong, J. M. Luther, Z. A. Li and Z. Zhu, Stabilized hole-selective layer for high-performance inverted p–i–n perovskite solar cells, *Science*, 2023, **382**, 284–289.

53 X. Lin, Y. Wang, H. Su, Z. Qin, Z. Zhang, M. Chen, M. Yang, Y. Zhao, X. Liu, X. Shen and L. Han, An *In Situ* Formed Tunneling Layer Enriches the Options of Anode for Efficient and Stable Regular Perovskite Solar Cells, *Nano-Micro Lett.*, 2022, **15**, 10.